AALBORG UNIVERSITY
DENMARK

An Integrated Inductor For Parallel Interleaved Three-Phase Voltage Source Converters

Gohil, Ghanshyamsinh Vijaysinh; Bede, Lorand; Teodorescu, Remus; Kerekes, Tamas; Blaabjerg, Frede

An Integrated Inductor For Parallel Interleaved Three-Phase Voltage Source Converters

Ghanshyamsinh Gohil, *Student Member, IEEE,* Lorand Bede, *Student Member, IEEE,*
Remus Teodorescu, *Fellow, IEEE,* Tamas Kerekes, *Member, IEEE,* and Frede Blaabjerg, *Fellow, IEEE,*

Abstract—Three phase Voltage Source Converters (VSCs) are often connected in parallel to realize high current output converter system. The harmonic quality of the resultant switched output voltage can be improved by interleaving the carrier signals of these parallel connected VSCs. As a result, the line current filtering requirement can be reduced. However, an additional inductive filter is required to suppress the circulating current. The integrated inductive component, which combines the functionality of the line filter inductor and the circulating current inductor is presented in this paper. An analysis of the flux density distribution in the integrated inductor is presented and design procedure is described. The analysis has been also verified by performing finite element analysis. The advantage offered by the use of the integrated inductor is demonstrated by comparing its volume with the volume of the state-of-the-art filtering solution. The performance of the integrated inductor is also verified by the experimental measurements.

Index Terms—Voltage source converters (VSC), parallel, interleaving, coupled inductor, integrated magnetics, line inductor, inductor, integrated, differential inductor

NOMENCLATURE

α Ratio of the maximum current ripple to the peak value of the fundamental frequency component of the current.

$\overrightarrow{I}$ Leg current vector.

$\overrightarrow{V}_{ref}$ Reference space voltage vector.

$\overrightarrow{V}_S$ Switched output voltage vector.

$\overrightarrow{V}$ Output voltage vector.

L Inductance matrix.

ΔI_x Ripple component of the resultant line current.

$\Delta I_{x,p_{max}}$ Worst case ripple component of the resultant line current.

$\Delta I_{x,p}$ Peak value of the ripple component of the resultant line current.

λ_{x_k} Flux linkage with kth coil of phase x.

λ_x Average value of the flux linkages of coils of phase x.

μ_0 Permeability of the air.

ϕ_x Common flux.

$\phi_{x,c_{max}}$ Maximum value of the circulating flux component.

$\phi_{x,c}$ Circulating flux component.

$\phi_{x_k,c}$ Circulating flux component that links with the kth coil of phase x.

$\phi_{x_k,f}$ Fundamental frequency component of the flux.

$\phi_{x_k,l_{max}}$ Worst case value of the common flux component.

$\phi_{x_k,l}$ Common flux component that links with the kth coil of the phase x.

$\phi_{x_k,r}$ Ripple component of the common flux.

$\phi_{x_{k_{max}}}$ Maximum value of the flux in the limbs.

ψ Reference voltage space vector angle (typically the grid voltage vector).

$\Re_g$ Reluctance of the air gap.

$\Re_l$ Reluctance of each of the limb.

$\Re_y$ Reluctance of the yoke.

$\Re_{by}$ Reluctance of the bridge yoke.

σ Interleaving angle.

θ Displacement power factor angle.

A_g Cross section area of the air gap.

A_w Area of each of the windows in the cell structure.

$A_{c,CI}$ Cross section area of the core of the Coupled Inductor (CI).

$A_{c,bl}$ Cross section area of the bridge leg.

$A_{c,l}$ Cross section area of the limb.

A_{cu} Cross section area of the coil.

$A_{w,CI}$ Window area of the CI.

$B_{m,bl}$ Maximum allowable value of the flux density in the bridge leg.

$B_{m,c}$ Maximum allowable value of the flux density in the cell.

f_c Carrier frequency.

I_x Resultant line current of phase x.

I_x, f Fundamental frequency component of the resultant line current.

$I_{x,p}$ Peak value of the fundamental frequency component I_x, f.

$I_{x_k,c}$ Circulating current component of the leg current I_{x_k}.

$I_{x_k,l}$ Common component of the leg current I_{x_k}.

I_{x_k} Leg current of phase x of the kth VSC.

J Current density.

K_s Stacking factor.

K_w Window utilization factor.

L_c Circulating current filter inductor.

L_f Line filter inductor.

l_g Length of the air gap.

M Modulation index.

N Number of turns in each coil.

n Total number of the parallel connected VSCs.

P Rated power of the parallel VSCs.

V_{dc} DC-link voltage.

V_{ph} RMS value of the rated phase voltage.

$V_{x_k o}$ Switched output voltage of phase x of the kth VSC with respect to the dc-link mid-point o.

$V_{x_v o}$ Averaged switched output voltage of phase x with respect to the common reference point o.

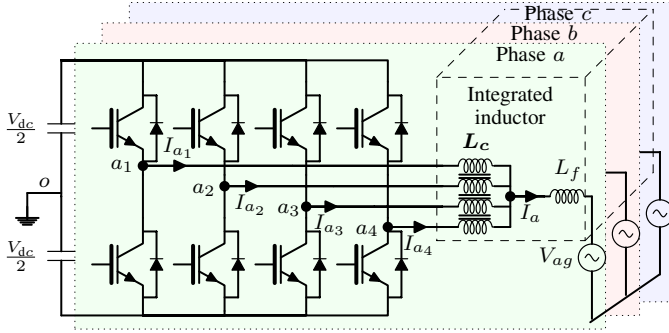V_{xg} RMS value of the grid voltage of phase x.

Fig. 1. Parallel interleaved voltage source converters with common dc-link ($n = 4$ in this illustration). Coupled inductor (CI) is used for suppressing the circulating current.

x Subscript, which represents phases a, b, and c.

x_c Common (output) terminal of the of phase x.

x_k Input terminal of the kth coil of phase x.

I. INTRODUCTION

Three-Phase Voltage Source Converter (VSC) is commonly used in many power electronics applications and often connected in parallel to realize medium/high power converter systems [1], [2]. The switching frequency of the semiconductor devices, used in medium/high power applications, is often limited [3]. Therefore, such systems may require large filter components to meet the stringent power quality requirements imposed by the utility [4]. The use of the large filter components occupy significant amount of space [5] and increase the cost of the overall converter system [6].

The size of the line filter components can be reduced by improving the output voltage waveform quality. In a system with parallel connected VSCs, this can be achieved by interleaving the carrier signals [7]–[12]. For a system with parallel connected VSCs, the resultant voltage of a given phase is the average of the switched output voltages of that phase of the individual VSCs. As a result of the interleaving of the carrier signals, the switched output voltages of the corresponding phase are shifted with respect to each other by an interleaving angle. Therefore, some of the harmonic frequency components present in the individual switched output voltages are either completely canceled or significantly reduced in the resultant output voltage. This helps to achieve the desired line current quality with relatively small line filter components. However, when connected to the common dc link, the circulating current flows between the parallel VSCs due to hardware and control asymmetries [13] and increases significantly when the carriers are interleaved [12]. This unwanted circulating current increases the stress on the semiconductor switches and causes additional losses. Therefore, it should be suppressed to some acceptable limits.

The circulating current can be avoided by providing galvanic isolation between the parallel VSCs using the multiple winding line frequency transformer [14]. However, the use of the bulky line frequency transformer adds to the cost and increases the size. Another approach is to suppress the circulating current to some acceptable limit by introducing

impedance in the circulating current path. This can be achieved by

1) Using Common-Mode (CM) inductor in series with the line filter inductor for each of the VSCs [8].
2) Using the Coupled Inductor (CI) to suppress the circulating current by providing magnetic coupling between the parallel interleaved legs of the corresponding phases [15]–[20] (refer Fig. 1).

In both of the above mentioned approaches, two distinct magnetic components are used:

1) Circulating current inductor L_c (CI / CM inductor).
2) Line filter inductor L_f (commonly referred to as a boost inductor) for improving the line current quality.

The volume of the inductive components can be reduced by integrating both of these functionalities into a single magnetic component. A single phase integrated inductor for the two parallel interleaved VSCs is proposed in [21]. The magnetic structure of this inductor has two side limbs and a central limb. Air gaps are introduced in all the three legs, out of which the length of the air gaps in both the side limbs are equal. The coils are placed around the side limbs and have equal number of turns. The flux in the magnetic core has two distinct components:

1) Flux component corresponding to the line filter inductor L_f (referred to as the common flux ϕ_x).
2) Flux component corresponding to the CI (referred to as the circulating flux $\phi_{x,c}$, which mainly confines to the side limbs).

The circulating flux component $\phi_{x,c}$ is given as

$$\phi_{x,c} = \frac{1}{2N} \int \left(V_{x_1 o} - V_{x_2 o} \right) dt \quad (1)$$

The maximum value of the circulating flux component is given as [22]

$$\phi_{x,c_{max}} = \frac{V_{dc}}{8N f_c} \quad (2)$$

The $\phi_{x,c_{max}}$ depends only on the dc-link voltage V_{dc}, the number of turns N, and the switching frequency f_c. Therefore, the introduction of the two air gaps in the magnetic path of the $\phi_{x,c}$ does not bring any advantage in terms of the size reduction (However depending upon the control scheme employed, small air gap may be needed to avoid the saturation). In addition, it is difficult to realize the inductor using the standard cores, when the length of the air gaps in the side limbs and the central limbs are different. Moreover, the solution presented in [21] is only applicable to two parallel interleaved VSCs. The circulating current suppression for three parallel VSCs is presented in [20]. Three limb magnetic core is used for the CIs and single phase inductors are employed for the line current filtering of each of the phases. The magnetic integration of all these components in a single magnetic structure can further reduce the volume of the overall system.

A three-phase integrated inductor for arbitrary number of parallel interleaved VSCs is proposed in this paper. The proposed integrated inductor combines the functionality of both the line filter inductor L_f and the circulating current inductor L_c. The magnetic structure and the detailed analysis
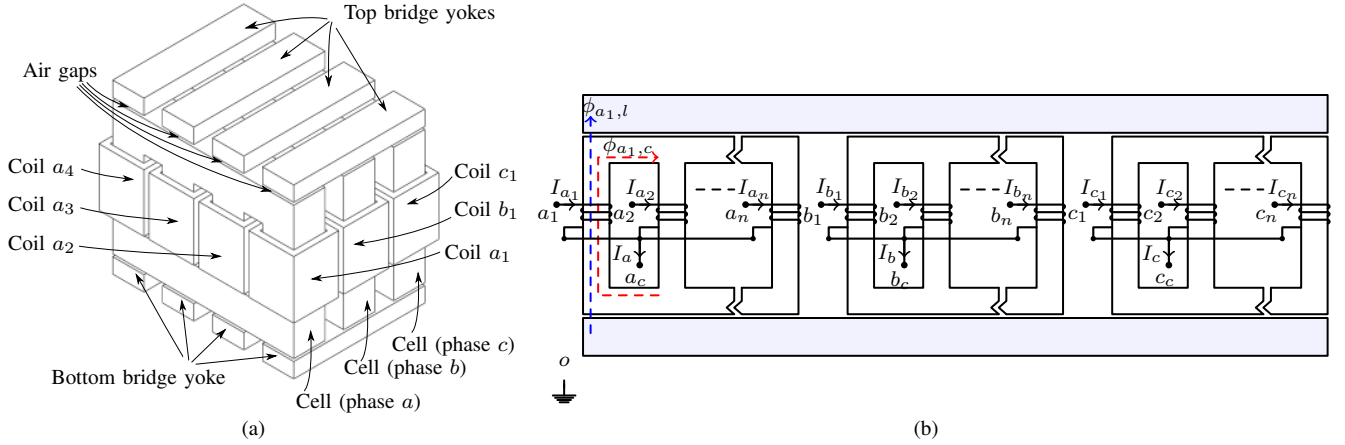
Fig. 2. Magnetic structure. (a) Magnetic structure of the proposed integrated three-phase inductor for n number of parallel connected VSCs ($n = 4$ in this illustration), (b) Alternative simplified arrangement.

of the proposed three-phase integrated inductor is presented in Section II. Section III, summarizes the design methodology of the integrated inductor. A comparison between the proposed inductor and the state-of-the-art solution, which uses a separate CIs for each of the phases and a three phase line filter inductor L_f, is also presented. Simulations and experimental results are given in Section IV.

II. INTEGRATED INDUCTOR

The magnetic structure, modeling and analysis of the proposed integrated inductor for n number of parallel interleaved VSCs is presented in this section.

A. Magnetic Structure

The magnetic structure of the proposed three-phase integrated inductor for n number of parallel VSCs is shown in Fig. 2(a) ($n = 4$ in the illustration). The simplified arrangement of the integrated inductor is also shown in Fig. 2(b). The magnetic core is composed of three identical magnetic structure belonging to each of the phases of the three-phase system. Such magnetic structure is referred to as a cell. Each cell contains n limbs, magnetically coupled to each other using the yokes, as shown in Fig. 2(a). Small inherent air gap exists when the limbs and the yokes are arranged together to form the cell structure. Therefore an intentional air gap is avoided (which otherwise may be needed to avoid saturation) to achieve high circulating current filter inductance L_c. Each limb carries a coil having N turns and all the coils are wound in the same direction. For a three phase system, three such cell are used, as shown in Fig. 2(a). The cells of all the three phases are magnetically coupled using the top and bottom bridge yokes. The necessary air gaps are inserted between the cells and the bridge yokes. The magnetic structure shown in Fig. 2(a) has six ventilation channels that can be used for guiding the air flow from bottom to top for better cooling.

The start terminal of the coils of a cell belonging to phase x is connected to the output terminal of the respective VSC leg x_k of the corresponding phase and the end terminal is connected to a common connection point of that phase x_c, as shown in Fig. 2(b). The magnetic structure, as shown in Fig.

2(a), is asymmetrical for $n > 2$. However, symmetrical cells can be realized using alternative cell structures, as shown in Fig. 3. In the interest of brevity, the analysis is presented for the symmetrical cell structure.
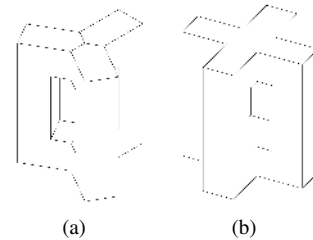

Fig. 3. Symmetrical magnetic cell structures for different number of parallel connected VSCs. (a) Three VSC case, (b) Four VSC case.

B. System Description

Referring to Fig. 2(b) and by neglecting the resistance of the coils, the switched output voltages (with respect to the fictitious mid-point of the dc-link o) are given as

$$\overrightarrow{V}_S = L \frac{d}{dt} \overrightarrow{I} + \overrightarrow{V} \tag{7}$$

where the corresponding current and voltage vectors and the inductance matrix L are given in (3), (4), (5), and (6) at the top of the next page.

Let the average of the switched output voltages of phase x be V_{x_vo} and it is represented as

$$V_{x_vo} = \frac{1}{n} \sum_{k=1}^{n} V_{x_ko}; \text{ where } 1 < k \leq n \tag{8}$$

The resultant line current of a particular phase is the sum of all leg currents of that phase and it is given as

$$I_x = \sum_{k=1}^{n} I_{x_k}; \text{ where } 1 \leq k \leq n \tag{9}$$

For the parallel interleaved VSCs, the leg current I_{x_k} can be split into two components:

1) The component contributing to the resultant line current $I_{x_k,l}$

$$\overrightarrow{V}_S = \begin{bmatrix} V_{a_1o} & V_{a_2o} \cdots & V_{a_no} & V_{b_1o} & V_{b_2o} \cdots & V_{bno} & V_{c_1o} & V_{c_2o} \cdots & V_{c_no} \end{bmatrix}^T \tag{3}$$

$$\overrightarrow{I} = \begin{bmatrix} I_{a_1} & I_{a_2} \cdots I_{a_n} & I_{b_1} & I_{b_2} \cdots I_{b_n} & I_{c_1} & I_{c_2} \cdots I_{c_n} \end{bmatrix}^T \tag{4}$$

$$\overrightarrow{V} = \begin{bmatrix} V_{a_co} & V_{a_co} \cdots & V_{a_co} & V_{b_co} & V_{b_co} \cdots & V_{b_co} & V_{c_co} & V_{c_co} \cdots & V_{c_co} \end{bmatrix}^T \tag{5}$$

$$\boldsymbol{L} = \begin{bmatrix}
L_{a_1a_1} & L_{a_1a_2} \cdots & L_{a_1a_n} & L_{a_1b_1} & L_{a_1b_2} \cdots & L_{a_1b_n} & L_{a_1c_1} & L_{a_1c_2} \cdots & L_{a_1c_n} \\
L_{a_2a_1} & L_{a_2a_2} \cdots & L_{a_2a_n} & L_{a_2b_1} & L_{a_2b_2} \cdots & L_{a_2b_n} & L_{a_2c_1} & L_{a_2c_2} \cdots & L_{a_2c_n} \\
\vdots & \vdots & \vdots & \vdots & \vdots & \vdots & \vdots & \vdots & \vdots \\
L_{a_na_1} & L_{a_na_2} \cdots & L_{a_na_n} & L_{a_nb_1} & L_{a_nb_2} \cdots & L_{a_nb_n} & L_{a_nc_1} & L_{a_nc_2} \cdots & L_{a_nc_n} \\
L_{b_1a_1} & L_{b_1a_2} \cdots & L_{b_1a_n} & L_{b_1b_1} & L_{b_1b_2} \cdots & L_{b_1b_n} & L_{b_1c_1} & L_{b_1c_2} \cdots & L_{b_1c_n} \\
L_{b_2a_1} & L_{b_2a_2} \cdots & L_{b_2a_n} & L_{b_2b_1} & L_{b_2b_2} \cdots & L_{b_2b_n} & L_{b_2c_1} & L_{b_2c_2} \cdots & L_{b_2c_n} \\
\vdots & \vdots & \vdots & \vdots & \vdots & \vdots & \vdots & \vdots & \vdots \\
L_{b_na_1} & L_{b_na_2} \cdots & L_{b_na_n} & L_{b_nb_1} & L_{b_nb_2} \cdots & L_{b_nb_n} & L_{b_nc_1} & L_{b_nc_2} \cdots & L_{b_nc_n} \\
L_{c_1a_1} & L_{c_1a_2} \cdots & L_{c_1a_n} & L_{c_1b_1} & L_{c_1b_2} \cdots & L_{c_1b_n} & L_{c_1c_1} & L_{c_1c_2} \cdots & L_{c_1c_n} \\
L_{c_2a_1} & L_{c_2a_2} \cdots & L_{c_2a_n} & L_{c_2b_1} & L_{c_2b_2} \cdots & L_{c_2b_n} & L_{c_2c_1} & L_{c_2c_2} \cdots & L_{c_2c_n} \\
\vdots & \vdots & \vdots & \vdots & \vdots & \vdots & \vdots & \vdots & \vdots \\
L_{c_na_1} & L_{c_na_2} \cdots & L_{c_na_n} & L_{c_nb_1} & L_{c_nb_2} \cdots & L_{c_nb_n} & L_{c_nc_1} & L_{c_nc_2} \cdots & L_{c_nc_n}
\end{bmatrix} \tag{6}$$

2) The circulating current $I_{x_k,c}$
and it can be represented as

$$I_{x_k} = I_{x_k,l} + I_{x_k,c} \tag{10}$$

The circulating current components $I_{x_k,c}$ do not contribute to the resultant line current. Therefore, (9) can be re-written as

$$I_x = \sum_{k=1}^{n} I_{x_k,l}; \text{ where } 1 \le k \le n \tag{11}$$

Assuming an equal line current sharing between the parallel VSCs, the common component of the leg current is obtained as

$$I_{x_k,l} = \frac{I_x}{n} \tag{12}$$

Once the current quantities are defined, the qualitative analysis of the magnetic couplings is presented by performing the finite element analysis and the inductances values of the matrix $\boldsymbol{L}$ are obtained by solving the reluctance network, which is discussed in following sub sections.

C. Finite Element Analysis

Due to the Pulse Width Modulation (PWM), the switched output voltage V_{x_ko} has undesirable harmonic frequency components in addition to the required fundamental frequency component. When the carrier signals are interleaved, some of the harmonic frequency components of the switched output voltages of the parallel interleaved legs are phase shifted with respect to each other, whereas the rest of the harmonic frequency components are in-phase [23], [24]. The effects of these two distinct voltage components on the flux density distribution in the integrated inductor is evaluated by performing finite element analysis of an integrated inductor for the three parallel interleaved VSCs. The magnetic structure of the integrated inductor is shown in Fig. 4.
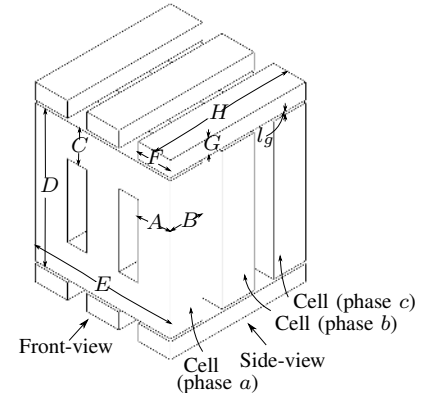

Fig. 4. Magnetic core geometry of the integrated inductor for the three parallel interleaved voltage source converters. The cross section area of the limb $A_{c,l} = A \times B \times K_s$. The cross section area of the bridge leg $A_{c,bl} = F \times G \times K_s$. The air gap area $A_g = B \times F$.

1) Effect of the In-phase Harmonic Frequency Components: All three coils of the phase a are excited by equal and in-phase fundamental frequency currents. The flux density vector distribution in this case is shown in Fig. 5, where the flux direction is indicated by the arrows. The flux density distribution in all three limbs of the cell is almost symmetrical and the flux linkage between the coils of the same phase is zero, as shown in Fig. 5(a). The flux due to the flow of the in-phase current in the kth coil of phase a, couples with the kth coils of the phase b and the phase c. For example, the induced flux due to the fundamental frequency component of I_{a_1} only links with coil b_1 and coil c_1 and completes its path through two air gaps and the corresponding top and bottom bridge yokes, as shown in Fig. 5(b). Therefore, the magnetic coupling coefficient between the kth coil of one of the phase and the jth coil of the other phase (where $k \ne j$) can be considered to be zero.
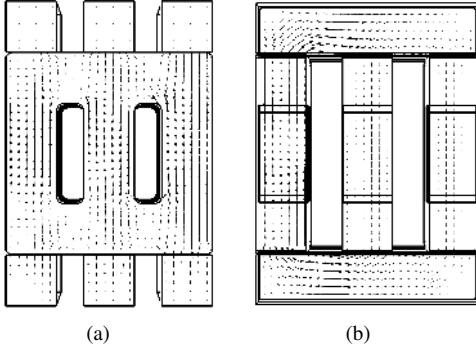
(a)   (b)

Fig. 5. Flux density vector distribution when the equal and in-phase fundamental frequency component of the current flows through the all three coils of phase A. (a) Cross-sectional view (front), (b) Cross-sectional view (side).
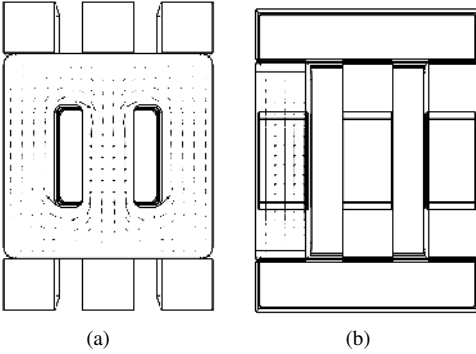

(a)   (b)

Fig. 6. Flux density vector distribution when the equal and symmetrically phase-shifted switching frequency component of the voltage applied across the all three coils of phase A. (a) Cross-sectional view (front), (b) Cross-sectional view (side).

2) Effect of the Phase Shifted Harmonic Frequency Components: Assuming symmetrical VSC legs, the magnitude of the harmonic frequency components in the switched output voltages of each of the interleaved legs is considered to be equal. If the interleaving angle σ between the successive carrier signals is taken to be the same $\sigma = 2\pi/n$ (symmetrical interleaving), then the effect of the phase shifted harmonic components is canceled in the resultant voltage [23], [24]. Therefore, the phase shifted harmonic frequency components only appears across the corresponding coils and does not influence the resultant output. The flux density vector distribution, when the switching frequency component with equal magnitude and symmetrical phase shift is applied across the coils of phase a, is shown in Fig. 6. The induced flux is mainly confined to the cell. For example, the induced flux due to the phase shifted component of the voltage across coil a_1 links with coil a_2 and coil a_3 and does not link with the coils of phase b and phase c. Similar argument applies to the phase b and the phase c.

Neglecting the leakage, the flux that links with each of the coils can be divided into two distinct components:

1) The flux component, which links with the corresponding coils of the other two phases (referred to as the common flux component $\phi_{x_k,l}$).
2) The flux component, which links with the remaining coils of the cell belonging to the same phase (referred to as a
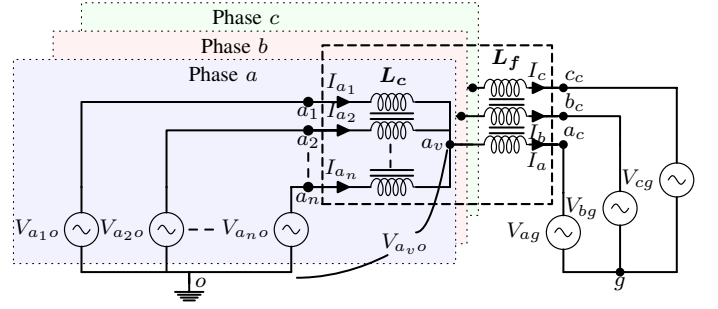

Fig. 7. Equivalent electrical circuit of the parallel interleaved VSCs with the proposed integrated inductor.

circulating flux component $\phi_{x_k,c}$).

Considering symmetrical cell structure, the inductances can be represented as

$$L_{a_j b_j} = L_{b_j c_j} = L_{c_j a_j} = -L_m \text{ for all } 1 \le j \le n \quad (13)$$

$$L_{a_j b_k} = L_{b_j c_k} = L_{c_j a_k} \cong 0$$
$$\text{for all } 1 \le j \le n, 1 \le k \le n, \text{ and } j \ne k \quad (14)$$

$$L_{x_j x_k} = -L_{m_1} \text{ for all } 1 \le j \le n, 1 \le k \le n, \text{ and } j \ne k \quad (15)$$

The $-ve$ sign is used to represent the L_m and L_{m_1} and the same convention has been followed through out the paper. Neglecting the leakage flux, the self-inductance of each of the coils is given as

$$L_{a_j a_j} = L_{b_j b_j} = L_{c_j c_j} = (n-1)L_{m_1} + 2L_m$$
$$\text{for all } 1 \le j \le n \quad (16)$$

D. Equivalent Electrical Circuit

By substituting these inductance values in (6) and averaging the pole voltages of each of the phase gives

$$\begin{bmatrix} V_{a_v o} - V_{a_c o} \\ V_{b_v o} - V_{b_c o} \\ V_{c_v o} - V_{c_c o} \end{bmatrix} = \frac{1}{n} \begin{bmatrix} 2L_m & -L_m & -L_m \\ -L_m & 2L_m & -L_m \\ -L_m & -L_m & 2L_m \end{bmatrix} \frac{d}{dt} \begin{bmatrix} I_a \\ I_b \\ I_c \end{bmatrix} \quad (17)$$

For the three-phase three-wire system, $I_a + I_b + I_c = 0$ and the inductance offered to the resultant line current is given as

$$L_f = \frac{V_{x_v o} - V_{x_c o}}{dI_x/dt} = \frac{3}{n} L_m \quad (18)$$

The behavior of the circulating current can be described by subtracting the averaged pole voltage from the pole voltages of the corresponding phases and further simplification of those equations give

$$\overrightarrow{V_{S_x}} = \boldsymbol{L_c} \frac{d}{dt} \overrightarrow{I_{x,c}} + V_{x_v o} \quad (19)$$

where

$$\overrightarrow{V_{S_x}} = \begin{bmatrix} V_{x_1 o} & V_{x_2 o} & \cdots & V_{x_n o} \end{bmatrix}^T \quad (20)$$

$$\overrightarrow{I_{x,c}} = \begin{bmatrix} I_{x_1,c} & I_{x_2,c} & \cdots & I_{x_n,c} \end{bmatrix}^T \quad (21)$$

$$\boldsymbol{L_c} = \begin{bmatrix} (n-1)L_{m_1} & -L_{m_1} & \cdots & -L_{m_1} \\ -L_{m_1} & (n-1)L_{m_1} & \cdots & -L_{m_1} \\ \vdots & \vdots & \vdots & \vdots \\ -L_{m_1} & -L_{m_1} & \cdots & (n-1)L_{m_1} \end{bmatrix}$$
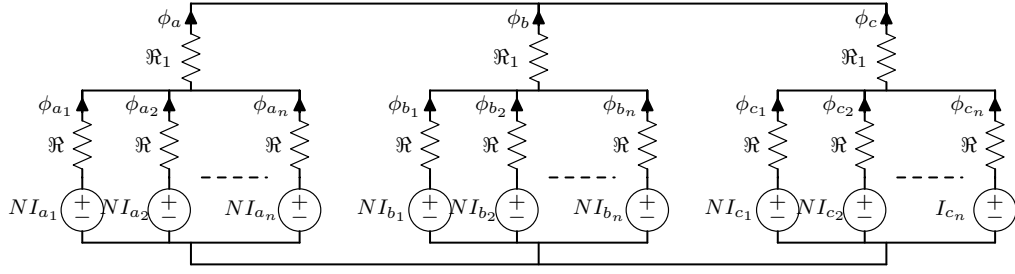$$(22)$$

Fig. 8. Simplified reluctance model of the three-phase inductor with symmetrical cells.

Using (18) and (19), the electrical equivalent circuit is obtained and it is shown in Fig. 7. Here x_v is the virtual common point and the potential of this point with respect to the mid-point of the dc-link is the averaged pole voltage $V_{x_v o}$. The potential difference of $V_{x_v o} - V_{x_c o}$ appears across the line filter inductor L_f, as shown in Fig. 7.

E. Reluctance Network

The relationship between the inductance values and the physical parameters of the integrated inductor is obtained by solving the reluctance network and presented in this sub section.

The simplified reluctance model of the three-phase integrated inductor with the symmetrical cells is shown in Fig. 8. The reluctance of each of the leg is $\Re$ and it is given as

$$\Re = \Re_l + \Re_y \tag{23}$$

The equivalent reluctance of the air gaps ($\Re_g$) and the bridge yoke ($\Re_{by}$) is represented by $\Re_1$ and can be written as

$$\Re_1 = \frac{2}{n}(\Re_g + \Re_{by}) \tag{24}$$

The reluctance of the air gaps is generally large compared to the reluctance of the bridge yoke. Therefore, $\Re_1$ can be approximated to be $\frac{2}{n}\Re_g$. By solving the reluctance network, the flux linking with each of the coils is given as

$$
\begin{aligned}
\lambda_{x_k}(t) &= \int \left(V_{x_k o} - V_{x_c o} \right) dt \\
&= \frac{N^2}{\Re + n\Re_1} \frac{I_x(t)}{n} + \frac{N^2}{\Re} I_{x_k,c}(t)
\end{aligned} \tag{25}
$$

Averaging the flux linkages of each of the phase group gives

$$
\begin{aligned}
\lambda_x(t) &= \frac{1}{n}\sum_{k=1}^{n} \lambda_{x_k} = \int \left(V_{x_v o} - V_{x_c o} \right) dt \\
&= \frac{N^2}{\Re + n\Re_1} \frac{I_x(t)}{n} + \frac{N^2}{\Re} \frac{1}{n}\sum_{k=1}^{n} I_{x_k,c}(t)
\end{aligned} \tag{26}
$$

As per the definition of the circulating current

$$\sum_{k=1}^{n} I_{x_k,c} = 0 \tag{27}$$

Using (18), (25), and (26), the inductance offered to the resultant line current is given as

$$L_f = \frac{N^2}{n(\Re + n\Re_1)} \tag{28}$$

since, $n\Re_1 >> \Re$, the line inductance can be given as

$$L_f \approx \frac{N^2}{n^2\Re_1} = \frac{N^2}{2n\Re_g} = \frac{\mu_0 N^2 A_g}{2n l_g} \tag{29}$$

As it is evident from (29), the line inductance value mainly depends on the geometry of the air gap.

The values of the circulating current inductance can be obtained by subtracting (26) from (25) as

$$
\begin{aligned}
\int \left(V_{x_k o} - V_{x_v o} \right) dt =& \frac{(n-1)}{n}\frac{N^2}{\Re} I_{x_k,c}(t) \\
&- \frac{1}{n}\frac{N^2}{\Re}\left(\sum_{\substack{j=1 \\ j\neq k}}^{n} I_{x_j,c}(t) \right)
\end{aligned} \tag{30}
$$

Using (19) and (30), the expression for L_{m_1} is obtained as

$$L_{m_1} = \frac{1}{n}\frac{N^2}{\Re} = \frac{1}{n}\frac{N^2}{\Re_l + \Re_y} \tag{31}$$

It is evident that L_{m_1} is independent of the air gap geometry and depends only on the reluctances of the limb and yokes (and the reluctance of the inherent air gaps). The value of the L_{m_1} and therefore the inductance offered to the circulating current can be increased by using high permeability magnetic material for the cells.

III. DESIGN AND VOLUMETRIC COMPARISON

The design methodology of the integrated inductor for grid-connected unity power factor application is presented in this section and the results are compared with the state-of-the-art solution of using three separate CIs and one three-phase line filter inductor. Design equations for three parallel interleaved VSCs are presented for the core geometry shown in Fig. 4. However, the design methodology presented in this paper is applicable to any number of parallel interleaved VSCs.

A. Pulse Width Modulation Scheme

The flux in the core is strongly influenced by the PWM scheme used [25]. The use of the center aligned Space Vector Modulation (SVM) is considered in this paper. Each of the VSCs cycles through four switch states in each switching cycle. Based on the position of the reference space vector ($\overrightarrow{V}_{ref}$), two adjacent active voltage vectors and both of the zero voltage vectors are applied to synthesize $\overrightarrow{V}_{ref}$. The carrier signals of the parallel VSCs are phase shifted with respect to each other by an interleaving angle $\sigma = 120°$.
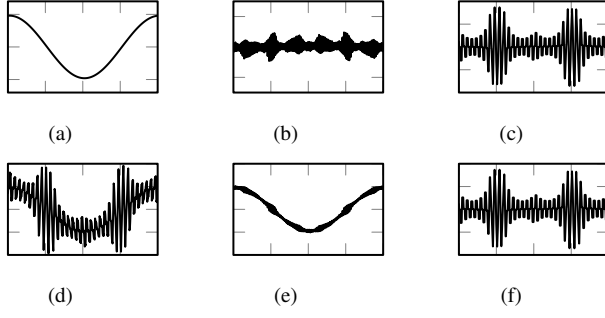
Fig. 9. Flux waveforms. (a) Fundamental component of the common flux $\phi_{x_k,f}$, (b) Ripple component of the common flux $\phi_{x_k,r}$, (c) Circulating flux component $\phi_{x_k,c}$, (d) Flux in the limbs $\phi_{x_k}(t) = \left(\phi_{x_k,f}(t) + \phi_{x_k,r}(t) + \phi_{x_k,c}(t)\right)$, (e) Flux in the bridge legs $\phi_{x_k,l}(t) = \left(\phi_{x_k,f}(t) + \phi_{x_k,r}(t)\right)$, (f) Flux in the yokes $\phi_{x_k,c}$.

B. Maximum Flux Values

The flux waveforms in various parts of the integrated inductor are shown in Fig. 9. The flux components can be classified into three categories:

1) Fundamental flux component $\phi_{x_k,f}$.
2) Ripple component of the flux $\phi_{x_k,r}$ with predominant harmonic frequency component of $3 \times f_c$.
3) Circulating flux component $\phi_{x_k,c}$ with predominant harmonic frequency component of f_c and $2 \times f_c$.

The flux in each limb is the vector addition of the $\phi_{x_k,l}$ and $\phi_{x_k,c}$, whereas the bridge yokes only experiences the flux of $\phi_{x_k,l}$. For the proper design of an integrated inductor, maximum value of these flux components are required and derived hereafter.

1) Common Flux Component: The common flux component can be obtained from (25) and it is given as

$$\phi_{x_k,l}(t) \approx \frac{\mu_0 N A_g}{2nl_g} I_x(t) \tag{32}$$

The resultant line current I_x is a combination of a fundamental frequency component I_x, f and a ripple component ΔI_x. Therefore, (32) can be re-written as

$$\phi_{x_k,l}(t) = \frac{\mu_0 N A_g}{2nl_g}\left(I_{x,p}\cos(\psi - \theta) + \Delta I_x(t)\right) \tag{33}$$

The maximum value of ΔI_x depends on the pulse-width modulation scheme, the modulation index M, the dc-link voltage V_{dc}, the switching frequency f_c [25], and the line filter inductor L_f. Considering the balanced three-phase system, the design equations for only phase a are derived. For the unity power factor applications, the fundamental component of the resultant line current is maximum for full load condition at $\psi = 0°$. The ripple component of the line current for $M > \frac{4}{9}$ at $\psi = 0°$ is given as

$$\Delta I_{a,p} \mid_{\psi=0°} = \frac{V_{dc}}{3L_f f_c}\left(\frac{5M}{8} - \frac{9M^2}{32} - \frac{1}{3}\right) \tag{34}$$

where the modulation index M is defined as
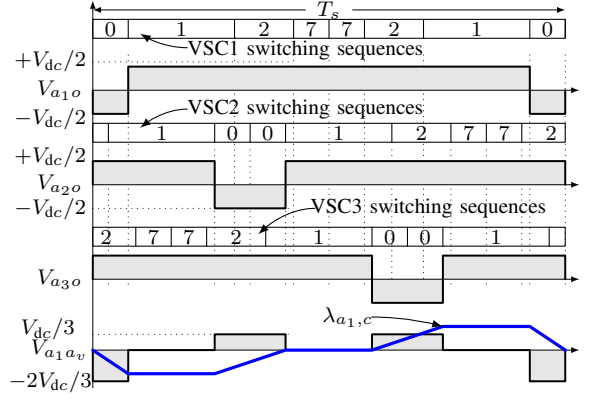
$$M = \frac{2\sqrt{2}V_{xg}}{V_{dc}} \tag{35}$$

Fig. 10. Space vector modulation: Switched output voltage of phase a of each of the individual VSCs and the voltage across coil a_1 when the carriers are interleaved by an interleaving angle of $120°$. The modulation index $M = \sqrt{3}/2$ and a space vector angle $\psi = 20°$.

The worst case value of the common flux component $\phi_{a_k,l_{max}}$ is

$$\begin{aligned}\phi_{a_k,l_{max}} &= \frac{\mu_0 N A_g}{2nl_g}\left(I_{x,p_{max}} + \Delta I_{x,p}\mid_{\psi=0°}\right)\\ &= \frac{\sqrt{2}L_f P}{3NV_{ph}} + \frac{V_{dc}}{3Nf_c}\left(\frac{5M}{8} - \frac{9M^2}{32} - \frac{1}{3}\right)\end{aligned} \tag{36}$$

2) Circulating Flux Component: Using (30), the circulating flux component in each limb $\phi_{x_k,c}$ is given as

$$\phi_{x_k,c}(t) = \frac{1}{N}\left(\frac{n-1}{n}\int V_{x_k o}\,dt - \frac{1}{n}\sum_{\substack{j=1\\j\neq k}}^{n}\int V_{x_j o}\,dt\right) \tag{37}$$

For $n = 3$, the flux linkage of coil a_1 due to the circulating flux component is given as

$$N\phi_{a_1,c}(t) = \frac{2}{3}\int V_{a_1 o}\,dt - \frac{1}{3}\int (V_{a_2 o} + V_{a_3 o})\,dt \tag{38}$$

The switching sequences and the switched output voltages of the phase a of all three VSCs are shown in Fig. 10. T_1, T_2, T_0 and T_7 are the dwell times of the voltage vectors $\overrightarrow{V}_1$, $\overrightarrow{V}_2$, $\overrightarrow{V}_0$, and $\overrightarrow{V}_7$, respectively. The flux linkage due to the circulating flux component in a given switching cycle is shown in Fig. 10 for the modulation index $M = \sqrt{3}/2$ and the space vector angle $\psi = 20°$. The peak value of the flux linkage is different in each switching cycle due to the change in the dwell times of the voltage vectors, as shown in Fig. 11. The flux linkage due to the circulating flux component is independent of the load and depends only on the modulation scheme, the dc-link voltage, and the switching frequency. The maximum value of the peak flux linkage occurs at the $\psi = 90°, 270°$ (refer Appendix) and it is given as

$$N\phi_{a_k,c_{max}} = \frac{V_{dc}}{9f_c} \tag{39}$$

Let the common-mode flux be

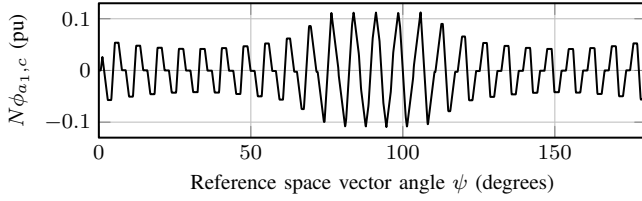$$\phi_{CM_1} = \frac{\phi_{a_1} + \phi_{b_1} + \phi_{c_1}}{3} \tag{40}$$

Fig. 11. Flux linkage due to the circulating flux component in a half fundamental frequency cycle for $m = \sqrt{3}/2$. The flux linkage is normalized with respect to $V_{dc}T_s$.

After some mathematical manipulation, this can be represented as

$$\phi_{CM_1} = \frac{\phi_{a_1,c} + \phi_{b_1,c} + \phi_{c_1,c}}{3} \tag{41}$$

From (41), it is clear that the common-mode flux component ϕ_{CM_1} of VSC1 is composed of the circulating flux component of all the phases of that VSC. As the low reluctance path for the circulating flux component of each of the phase exists in the proposed structure, high value of the inductance for the common-mode circulating current is also achieved.

3) Maximum Flux in Various Parts of the Integrated Inductor: For the unity power factor applications considered in this paper, the resultant flux component $\phi_{a_k,l}$ reaches the maximum value at $\psi = 0°$, whereas $\phi_{a_k,c}$ attains maximum value at $\psi = 90°$. The total flux in the limbs of the integrated inductor is a vector sum of the $\phi_{a_k,l}$ and the $\phi_{a_k,c}$. Therefore, the maximum value of the flux in the limbs is given as

$$\phi_{a_{k_{max}}} = \max\left(\phi_{a_k} \mid_{\psi=0°}, \phi_{a_k} \mid_{\psi=90°}\right) \tag{42}$$

The circulating flux component at $\psi = 0°$ is given as (refer Appendix)

$$\phi_{a_k,c} \mid_{\psi=0°} = \begin{cases} \frac{V_{dc}}{9Nf_c}, & 0 \leqslant M < \frac{4}{9} \\ \frac{(4-3M)V_{dc}}{24Nf_c}, & \frac{4}{9} \leqslant M < \frac{2}{\sqrt{3}} \end{cases} \tag{43}$$

In most grid connected applications, the modulation index varies in a small range around 1. Once the range of the modulation index is defined, the maximum value of $\phi_{a_k,c} \mid_{\psi=0°}$ can be obtained using (43). The flux in the limb at $\psi = 0°$ can be obtained using (36) and (43) and it is given as

$$\phi_{a_k} \mid_{\psi=0°} = \phi_{a_k,l_{max}} + \phi_{a_k,c} \mid_{\psi=0°} \tag{44}$$

Similarly, the flux in the limb at $\psi = 90°$ is given as

$$\phi_{a_k} \mid_{\psi=90°} = \phi_{a_k,c_{max}} + \phi_{a_k,l} \mid_{\psi=90°} \tag{45}$$

The value of the common component of the flux at $\psi = 90°$ is

$$\phi_{a_k,l} \mid_{\psi=90°} = \frac{V_{dc}}{18Nf_c}\left(\frac{2}{3} - \frac{\sqrt{3}M}{4}\right) \tag{46}$$

Using (39), (45), and (46), the flux in the limb at $\psi = 90°$ is given as

$$\phi_{a_k} \mid_{\psi=90°} = \frac{V_{dc}}{18Nf_c}\left(\frac{8}{3} - \frac{\sqrt{3}M}{4}\right) \tag{47}$$

Values of the $\phi_{a_k} \mid_{\psi=0°}$ and $\phi_{a_k} \mid_{\psi=90°}$ are calculated using (44) and (47), respectively. From these values, $\phi_{a_{k_{max}}}$ can be obtained using (42). The common flux component completes

its path through the bridge yokes and corresponding legs of the other two phases. Therefore, the maximum value of the flux component in the bridge yokes is $\phi_{a_k,l_{max}}$ and can be obtained by using (36).

C. Design Methodology

The steps toward the design of the integrated inductor are described in this sub section.

1) Calculation of the Line Filter Inductance L_f: The required value of the line filter inductance L_f can be calculated based on the permissible value of the ripple component of the resultant line current and it is given as

$$L_f = \frac{V_{dc}}{18\Delta I_{x,p_{max}}f_c}\left(\frac{2}{3} - \frac{\sqrt{3}M}{4}\right) \tag{48}$$

Let α be the ratio of the maximum current ripple to the peak value of the fundamental frequency component of the current and it can be written as

$$\alpha = \frac{\Delta I_{x,p_{max}}}{I_{x,p}} \tag{49}$$

Substituting (35) and (49) in (48), the inductance value at rated grid voltage can be obtained as

$$L_f = \frac{V_{dc}}{18\alpha I_{x,p}f_c}\left(\frac{2}{3} - \frac{2\sqrt{6}V_{ph}}{4V_{dc}}\right) \tag{50}$$

2) Area Product Requirement: The product of the cross section area of the limb $A_{c,l}$ and the window area A_w is referred to as an area product in this paper and it is used for the design of the integrated inductor.

The ripple component in the common flux component is very small compared to the ripple of the circulating flux component and its effect in the total flux can be neglected. In this case, the magnetic flux density in the limb at $\psi = 0°$ and $\psi = 90°$ can be obtained from (44) and (47), respectively. The values of the flux densities are

$$B_{a_k} \mid_{\psi=0°} = \frac{2V_{dc}(2+9\alpha)-3\sqrt{6}V_{ph}(1+3\sqrt{3}\alpha)}{108N\alpha A_{c,l}f_c} \tag{51a}$$

$$B_{a_k} \mid_{\psi=90°} = \frac{16V_{dc}-3\sqrt{6}V_{ph}}{108NA_{c,l}f_c} \tag{51b}$$

The values of the $B_{a_k} \mid_{\psi=0°}$ and $B_{a_k} \mid_{\psi=90°}$ should be less than the maximum allowable value of the flux density $B_{m,c}$. Each window in the integrated inductor receives two coils with the same number of turns. The circulating current is suppressed effectively and its contribution in the rms value of the total current can be neglected. In this case, the number of turns can be expressed as

$$N = \frac{3K_w A_w J}{2I_x} \tag{52}$$

Using (51) and (52), the area product requirements to ensure that the maximum value of the flux density remains within the maximum allowable value $B_{m,c}$. These values can be expressed as

$$(A_{c,l}A_w) \mid_{\psi=0°} = \frac{I_x\left[2V_{dc}(2+9\alpha)-3\sqrt{6}V_{ph}(1+3\sqrt{3}\alpha)\right]}{162\alpha B_{m,c}K_w Jf_c} \tag{53a}$$

$$(A_{c,l}A_w) \mid_{\psi=90°} = \frac{I_x[16V_{dc}-3\sqrt{6}V_{ph}]}{162B_{m,c}K_w Jf_c} \tag{53b}$$

TABLE I
SYSTEM SPECIFICATIONS

Parameters	Values
No. of parallel VSCs n	3
Power P	15 kW
Switching frequency f_s	1.65 kHz
AC voltage (line-to-line)	400 V
DC-link voltage V_{dc}	650 V
Line filter inductor L_f	0.85 mH

TABLE II
CONSTANTS USED FOR THE DESIGN OF THE INTEGRATED INDUCTOR

Constants	α	$B_{m,c}$	$B_{m,bl}$	J	K_w	K_s
Values	0.2	0.9 T	1 T	2 A/mm^2	0.5	0.89

The area product requirement is given as

$$A_{c,l}A_w = \max\left((A_{c,l}A_w)\mid_{\psi=0^\circ}, (A_{c,l}A_w)\mid_{\psi=90^\circ} \right) \quad (54)$$

3) Core Selection for the Cell and Number of turns: Based on the computed value of the area product $A_{c,l}A_w$, the suitable core should be selected. Once the cross section area of the limb $A_{c,l}$ is know, the number of turns can be obtained from (51) and it can be given as

$$N = \frac{2V_{dc}(2+9\alpha) - 3\sqrt{6}V_{ph}(1+3\sqrt{3}\alpha)}{108B_{m,c}\alpha A_{c,l}f_c} \quad (55)$$
$$\text{for } B_{a_k}\mid_{\psi=0^\circ} > B_{a_k}\mid_{\psi=90^\circ}$$

or

$$N = \frac{16V_{dc} - 3\sqrt{6}V_{ph}}{108B_{m,c}A_{c,l}f_c} \quad (56)$$
$$\text{for } B_{a_k}\mid_{\psi=90^\circ} > B_{a_k}\mid_{\psi=0^\circ}$$

4) Core Selection for the Bridge Legs: The cross section area of the bridge leg is obtained from the (36) and it can be given as

$$A_{c,bl} = \frac{\phi_{a_k,l_{max}}}{B_{m,bl}} \quad (57)$$

5) Air Gap Geometry: The geometry of the air gap is obtained form (29) as

$$\frac{A_g}{l_g} = \frac{6L_f}{\mu_0 N^2} \quad (58)$$

The air gap area A_g depends on the dimensions of the cell and the bridge legs, as shown in Fig. 4. Once A_g is known, the value of l_g can be obtained using (58). In case of the requirement of the large air gap, several discrete air gaps can be realized using the core blocks that can be placed between the cells and the bridge yokes.

D. Design Example

An integrated inductor is designed for the three parallel interleaved VSCs. The system specifications are given in Table I. A laminated steel with 0.35 mm lamination thickness is used for the bridge yokes, whereas the cells are made up of amorphous metal alloy. Each of the coils has 81 number of turns ($N = 81$). Various constants, that are used in the design,

TABLE III
PARAMETERS OF THE DESIGNED INDUCTOR. ALL DIMENSIONS ARE IN MM. UNIT OF THE AREA IS MM^2. SEE FIG. 4 FOR DEFINITIONS.

Parameters	A, C, F	B	D	E	G	H	l_g	A_{cu}
Values	30	25	135	120	12	105	1.2	3.3

are specified in Table II. The geometrical parameters of the designed integrated inductor, defined in Fig. 4, are listed in Table III. The cell structure is realized using the rectangular blocks of the amorphous alloy and six inherent air gap exists in the cell structure. This would influence the value of the circulating current inductance $\boldsymbol{L_c}$. For the brevity, the analysis presented in section II assumes symmetrical cell structure, whereas the cell structure is asymmetrical in the realized integrated inductor. The circulating current inductance $\boldsymbol{L_c}$ of the realized inductor is calculated using the finite element analysis and it is found to be

$$\boldsymbol{L_c} = \begin{bmatrix} 11.48 & -5.97 & -5.03 \\ -5.97 & 12.32 & -5.92 \\ -5.03 & -5.92 & 11.48 \end{bmatrix} \text{mH} \quad (59)$$

The inherent air gap is taken to be 0.15 mm for this finite element analysis.

E. Volumetric Comparison

The advantages offered by the proposed integrated inductor is demonstrated by comparing it with the system with three separate CIs and a three phase line filter inductor L_f. Such system is shown in Fig. 1. Separate CI is used for each of the phases. For $n = 3$, three limb magnetic structure is required. Similarly, three limb magnetic structure is used for the line filter inductor. The area product approach is used to design these components as well. The maximum value of the flux density B_m and the current density J are assumed to be the same in both the cases.

1) Three Limb Coupled Inductor: Using (39) and (56), the area product of the CI is obtained as

$$(A_{c,CI}A_{w,CI}) = \frac{2I_xV_{dc}}{27B_{m,c}K_wJf_c} \quad (60)$$

For the integrated inductor, where $(A_{c,l}A_w)\mid_{\psi=0^\circ} < (A_{c,l}A_w)\mid_{\psi=90^\circ}$, the ratio of the area product of the integrated inductor to the area product of the CI can be obtained from (53) and (60) and it can be written as

$$\frac{(A_{c,l}A_w)\mid_{\psi=90^\circ}}{(A_{c,CI}A_{w,CI})} = 1 + \frac{4 - 3\sqrt{6}\frac{V_{ph}}{V_{dc}}}{12} \quad (61)$$

For the system parameters specified in Table I, the area product of the integrated inductor is 11.6% higher than that of the CI. However, the state-of-the-art solution requires line filter inductor L_f and the area product requirement of the L_f is discussed in the subsequent text.
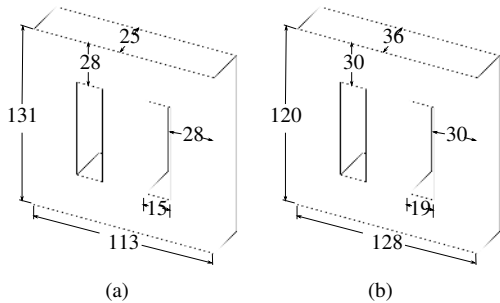
Fig. 12. Dimensions of the magnetic cores in millimeter. (a) Coupled inductor, (b) Line filter inductor.

TABLE IV
COIL PARAMETERS OF THE CI AND L_f

Parameters	CI	L_f
No. of turns N	78	27
Required copper area A_{cu}	3.3 mm^2	10.52 mm^2

TABLE V
VOLUME COMPARISON OF INTEGRATED INDUCTOR WITH A COMBINATION OF THREE CIs AND L_f

Volume (in ltr.)	Integrated inductor	Three CIs + L_f	% Change
Copper	0.322	0.44	73%
Amorphous alloys	1.046	0.947	110%
Laminated steel	0.226	0.470	48%
Total	1.594	1.857	85%

2) Three Phase Line Filter Inductor L_f: The area product of the three phase line filter inductor L_f is given as

$$(A_{c,L_f} A_{w,L_f}) = \frac{I_x(4V_{dc} - 3\sqrt{6}V_{ph})}{54 B_{m,bl}\alpha K_w J f_c} \quad (62)$$

Both the CI and three phase line filter inductor are designed using the area product approach. The dimensions of the magnetic cores are shown in Fig. 12. The number of turns and the cross section area of the coil for both the CI and the three phase inductor L_f are given in Table IV.

The volume of the different materials in case of both the solutions are calculated and the results are presented in Table V. For the system parameters considered in this paper, the use of integrated inductor results in a volume reduction of the copper by 27% and a volume reduction of the laminated steel by 52%. However, the volume of the amorphous alloys increases by 10%. The total volume the integrated inductor is 15% less than that of the state-of-the-art solution.

IV. SIMULATIONS AND EXPERIMENTAL RESULTS

A. Simulation Study

Time domain simulations have been carried out using the PLECS for the system parameters specified in Table I and Table III. The flux density waveforms in various parts of the integrated inductor are shown in Fig. 13. The flux in the limb of the integrated inductor is ensemble of the of the fundamental frequency flux component, the circulating flux component (with dominant frequency components at f_c and $2 \times f_c$), and the ripple component of the common flux
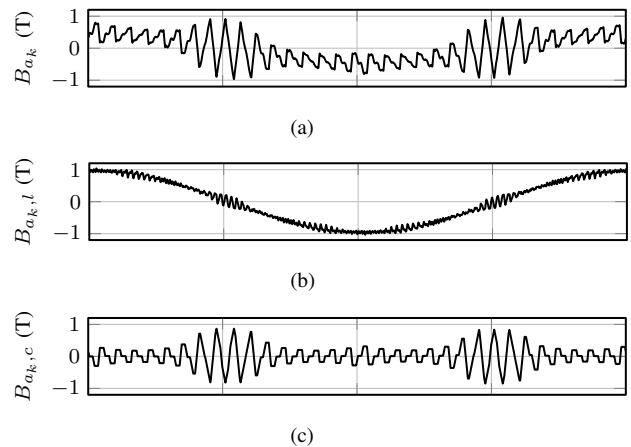

Fig. 13. Flux density waveforms in various parts of the integrated inductor. (a) Flux density in the limb, (b) Flux density in the bridge leg, (c) Flux density in the yoke.
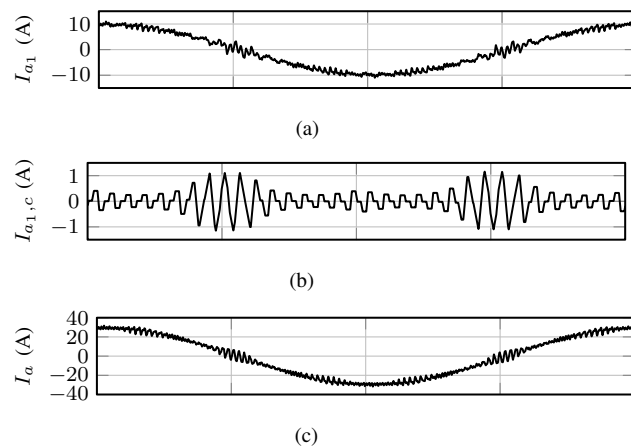

Fig. 14. Current waveforms of phase a. (a) Leg current of VSC1, (b) Circulating current of VSC1, (c) Resultant line current.

(with dominant frequency component at $3 \times f_c$), as shown in Fig. 13(a). Out of these, the common flux components flow through the bridge yokes, as shown in Fig. 13(b), whereas the circulating flux component is mainly confined in the cell and flows through the yokes, as shown in Fig. 13(c). The peak values of the flux density in various parts of the integrated inductor matches with the analysis presented in this paper. The simulated current waveforms are shown in Fig. 14. The integrated inductor suppresses the circulating current and offers the desired inductance to the resultant line current as shown in Fig. 14(b) and Fig. 14(c), respectively.

B. Hardware Results

The integrated inductor was designed and built for the system specified in Table I and the photograph of the implemented inductor is shown in Fig. 15. The parameters of the integrated inductor are given in Table III. The cells were made from amorphous alloys, whereas laminated steel was used for the bridge legs. The coils are wound using the AWG 12 copper wire. The dc side of the three parallel VSCs were connected to the common dc supply of 650 V. The control was
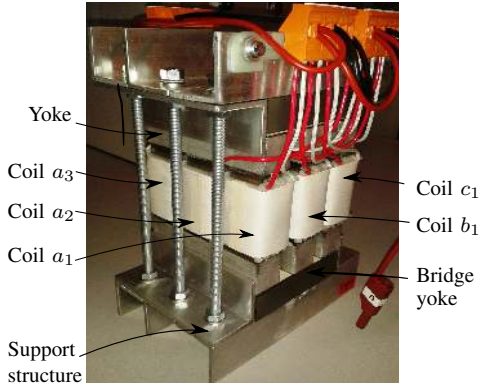
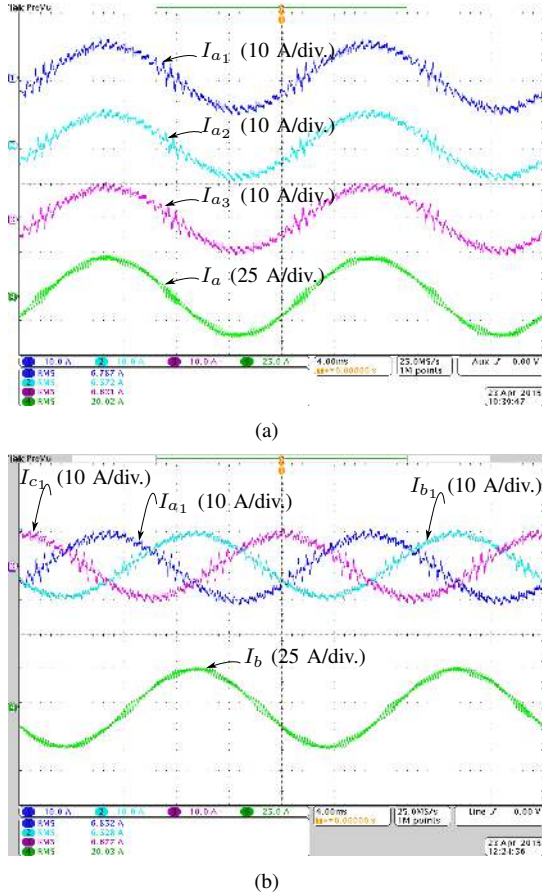Fig. 15. Photograph of the implemented integrated inductor.

(a)

(b)

Fig. 16. Experimental waveforms. (a) Ch1: phase a current of VSC1 I_{a_1}, Ch2: phase a current of VSC2 I_{a_2}, Ch3: phase a current of VSC3 I_{a_3}, Ch4: Resultant line current of phase a I_a, (b) Ch1: phase a current of VSC1 I_{a_1}, Ch2: phase b current of VSC1 I_{b_1}, Ch3: phase c current of VSC3 I_{c_1}, Ch4: Resultant line current of phase b I_b.

implemented using the TMS320F28346 floating point digital signal processor. The carrier signals of the three VSCs were interleaved by $120°$ and the line currents are sampled and the control loop is executed on every top and bottom update of each of the carrier signals.

The VSCs were operated to inject rated line current. The phase a currents of all the VSCs along with the resultant line current are shown in Fig. 16(a). The integrated inductor offers desired line filtering to the resultant current, which is evident
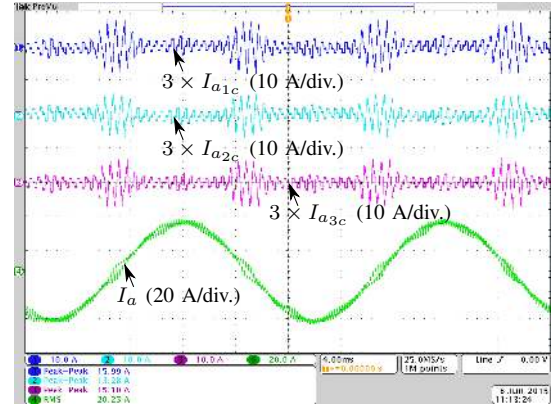

Fig. 17. Experimental waveforms of the scaled circulating currents of phase a. The captured circulating current waveforms are $3 \times I_{a_{kc}}$. (a) Ch1: Scaled version of the circulating current of VSC1 ($3 \times I_{a_{1c}}$), Ch2: Scaled version of the circulating current of VSC2 ($3 \times I_{a_{1c}}$), Ch3: Scaled version of the circulating current of VSC3 ($3 \times I_{a_{1c}}$), Ch4: Resultant line current of phase a I_a.
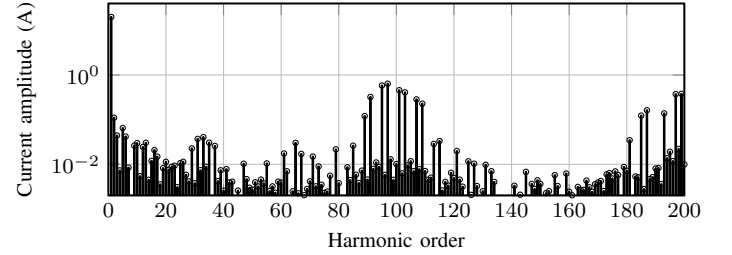

Fig. 18. Harmonic spectra of the resultant line current I_a. Total harmonic distortion of the I_a is 4.85%.

from Fig. 16(a). The current waveforms of all three phases of the VSC1 are also shown in Fig. 16(b). The circulating current component is defined as the $I_{a_{kc}} = I_{a_k} - (I_a/3)$. As it is difficult to measure these quantities, the scaled version is measured, which is three times more than the actual circulating current and it is measured by passing three turns of the conductor carrying I_{a_k} and one turn of the conductor carrying current I_a through the current probe. The difference of these two currents is obtained by arranging these conductors in such a manner that the current in them flows in opposite direction to each other. The scaled version of the circulating current components of each of the VSCs ($3 \times I_{a_{kc}}$) are shown in Fig. 17, which demonstrates that the integrated inductor effectively suppresses the circulating current. Peak value of the circulating current is restricted to 20% of the amplitude of the fundamental component of the rated value of the individual VSC current.

The harmonic spectra of the resultant line current I_a is shown in Fig. 18. The major harmonic component appears at the $3 \times f_c$ and the magnitude of the harmonic components in the resultant line current is significantly small due to the inductance L_f offered by the integrated inductor. The total harmonic distortion of the I_a is measured to be 4.85 %, which proves the effectiveness of the integrated inductor.
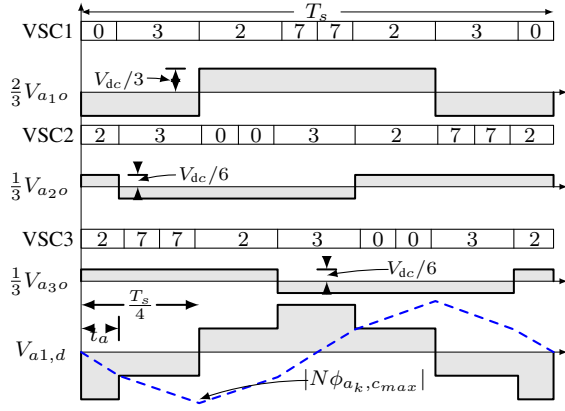
Fig. 19. Switching sequences of all three VSCs and their pole voltages for the interleaving angle of $120°$ and space vector angle of $psi = 90°$. The voltage that is responsible for the circulating flux component that links with the coil a_1 ($V_{a1,d} = \frac{2}{3}V_{a_1o} - \frac{1}{3}V_{a_2o} - \frac{1}{3}V_{a_3o}$) is also shown. The numbers represent the time during which the corresponding voltage vectors are applied.

V. CONCLUSION

An integrated inductor for parallel interleaved VSCs is presented in this paper. The proposed inductor integrates the functionality of three CIs and a three phase line filter inductor. The detailed analysis of the flux density distribution in various parts of the integrated inductor is presented and the analysis has been verified by the finite element analysis and the time domain simulations. The design methodology has been illustrated and the integrated inductor for the three parallel interleaved VSCs has been designed. The advantage offered by the integrated inductor in terms of the size reduction is demonstrated by comparing the volume of the integrated inductor with the state-of-the-art solution of using three CIs and the three phase line filter inductor. For the system considered in this paper, the total volume of the material is reduced by 15% by using the integrated inductor. The performance of the integrated inductor is also verified by carrying out the experimental measurements.

APPENDIX

A. Derivation of Circulating Flux Component

For $n = 3$, the flux linkage of coil a_1 due to the circulating flux component is given by (38). The switched output voltages of phase a of individual VSCs (after multiplying the appropriate coefficients given in (38)) at the $\psi = 90°$ are shown in Fig. 19. The voltage that is responsible for the circulating flux component that links with the coil a_1 ($\frac{2}{3}V_{a_1o} - \frac{1}{3}V_{a_2o} - \frac{1}{3}V_{a_3o}$) is also shown. The time integral of this voltage gives the flux linkage and it is shown by the dashed line in Fig. 19. The flux linkage achieves maximum value at time $t = T_s/4$. In this interval, the flux linkage can be described by the Piece-Wise Linear Equations (PWLE) and it is given as

$$N\phi_{a_1,c}(t) \mid_{\psi=90°} = N\phi_{a_1,c}(t_0) - \frac{2}{3}V_{dc}t \; ; \; 0 \le t < t_a$$
$$= N\phi_{a_1,c}(t_a) - \frac{1}{3}V_{dc}(t - t_a) \; ; \; t_a \le t < \frac{T_s}{4} \quad (63)$$
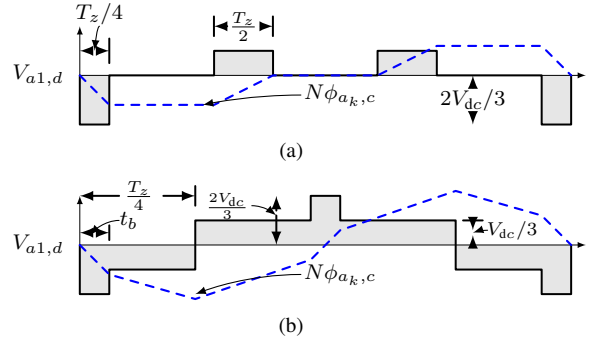

(a)

(b)

Fig. 20. voltage that is responsible for the circulating flux component that links with the coil a_1 ($V_{a1,d} = \frac{2}{3}V_{a_1o} - \frac{1}{3}V_{a_2o} - \frac{1}{3}V_{a_3o}$) at voltage space vector angle $\psi = 0°$. T_z is the dwell time of the zero voltage vector. (a) $T_1 > T_s/3$, (b) $T_1 < T_s/3$.

where $t_a = \frac{T_7}{2} + \frac{T_2}{2} - \frac{T_s}{6}$ and T_2 and T_7 are the dwell time of the voltage vectors $\overrightarrow{V}_2$ and $\overrightarrow{V}_7$, respectively. For the space vector angle $\psi = 0°$, $\frac{T_7}{2} + \frac{T_2}{2} = \frac{T_s}{4}$. Therefore, $t_a = \frac{T_s}{12}$. Substituting this value of t_a in (63) yields

$$N\phi_{a_1,c}(t_a) \mid_{\psi=90°} = -\frac{V_{dc}T_s}{18}$$
$$N\phi_{a_1,c}(\frac{T_s}{4}) \mid_{\psi=90°} = -\frac{V_{dc}T_s}{9} \quad (64)$$

Since the $N\phi_{a_1,c}(t)$ is maximum at $t = T_s/4$ for $\psi = 0°$, the maximum value of the peak flux linkage is given as

$$N\phi_{a_k,c_{max}} = \frac{V_{dc}}{9f_c} \quad (65)$$

Similarly, the voltage that is responsible for the circulating flux component that links with the coil a_1 ($\frac{2}{3}V_{a_1o} - \frac{1}{3}V_{a_2o} - \frac{1}{3}V_{a_3o}$) for voltage space vector angle $\psi = 0°$ can be obtained. However, this voltage waveforms are different for the $T_1 < T_s/3$ ($0 \le M < \frac{4}{9}$) and for the $T_1 > T_s/3$ ($\frac{4}{9} \le M < \frac{2}{\sqrt{3}}$). The voltage waveforms for both of these conditions are shown in Fig. 20.

For the $T_1 > T_s/3$ ($\frac{4}{9} \le M < \frac{2}{\sqrt{3}}$), the flux linkage is maximum at $t = T_z/4$ and its value is given as

$$N\phi_{a_1,c}(\frac{T_z}{4}) \mid_{\psi=0°} = \frac{1}{6}V_{dc}T_z \quad (66)$$

where T_z is the dwell time of the zero voltage vector. For the space vector angle $\psi = 0°$, $T_z = T_s - T_1$ and $T_1 = \frac{3}{4}MT_s$. Substituting this values in (66), yields

$$\phi_{a_1,c} \mid_{\psi=0°} = \frac{(4 - 3M)V_{dc}}{24Nf_c}, \; \frac{4}{9} \le M < \frac{2}{\sqrt{3}} \quad (67)$$

For the $T_1 < T_s/3$ ($0 \le M < \frac{4}{9}$), the flux linkage is maximum at $t = T_z/4$, as shown in Fig. 20(b). The flux linkage can be described by the PWLE and it is given as

$$N\phi_{a_1,c}(t) \mid_{\psi=0°} = N\phi_{a_1,c}(t_0) - \frac{2}{3}V_{dc}t \; ; \; 0 \le t < t_b$$
$$= N\phi_{a_1,c}(t_b) - \frac{1}{3}V_{dc}(t - t_b) \; ; \; t_b \le t < \frac{T_z}{4} \quad (68)$$

where t_b is given as

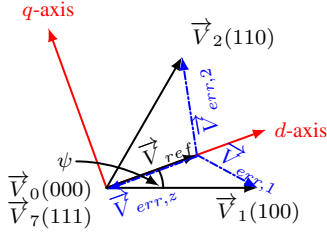$$t_b = (\frac{1}{3} + \frac{3M}{4})\frac{T_s}{4} \quad (69)$$

Fig. 21. Active and zero vectors that are used to synthesize the reference voltage space vector of one of the VSCs and corresponding error voltage vectors.

and T_z is given as

$$T_z = (1 - \frac{3M}{4})T_s \tag{70}$$

substituting the values of t_b and T_z in (68) yields

$$N\phi_{a_1,c}(t_b) \mid_{\psi=0°} = -(\frac{1}{3} + \frac{3M}{4})\frac{V_{dc}}{6f_c}$$
$$N\phi_{a_1,c}(\frac{T_z}{4}) \mid_{\psi=0°} = -\frac{V_{dc}}{9f_c}, \ 0 \leqslant M < \frac{4}{9} \tag{71}$$

B. Derivation of Common Component of Flux

The VSC synthesize the reference voltage space vector using the discrete voltage vectors. Therefore at any given instant, an error between the applied voltage vector and the reference voltage vector exists. The error voltage vectors for a given sampling instant for one of the VSCs are shown in Fig. 21. The time integral of the error voltage vectors gives the flux linkage of the line filter inductor. For the parallel interleaved VSCs, the flux linkage due to the ripple component of the common flux is the average of the time integral of the error voltage vectors of all three VSCs, as given in (26).

In the reference frame, rotating synchronously at the fundamental frequency, the instantaneous error voltage vectors can be decomposed into d-axis and the q-axis components and the decomposed error voltage vectors corresponding the active and zero vectors are given as

$$\overrightarrow{V}_{err,1} = \frac{2}{3}V_{dc}\big\{(\cos\psi - \frac{3}{4}M) - j\sin\psi\big\}$$
$$\overrightarrow{V}_{err,2} = \frac{2}{3}V_{dc}\{\cos(60° - \psi) - \frac{3}{4}M + j\sin(60° - \psi)\}$$
$$\overrightarrow{V}_{err,z} = -\frac{1}{2}V_{dc}M$$
$$\tag{72}$$

where the real part represents the d-axis component of the error voltage vector and the q-axis component is represented by an imaginary part. The average of the time integration of the error voltage vectors gives the ripple component of the common flux linkage $\Delta\lambda_d$ and $\Delta\lambda_q$. The fundamental component of the common flux appears as a dc component in the frame, rotating synchronously at the fundamental frequency. The dc components of both d-axis and q-axis (λ_D, λ_Q) flux are assumed to be constant during each sampling interval. Therefore, the d-axis and q-axis flux components in the rotating reference frame can be represented as

$$\lambda_d = \lambda_D + \Delta\lambda_d \text{ and } \lambda_q = \lambda_Q + \Delta\lambda_q \tag{73}$$

For the unity power factor applications, the dc components of both d-axis and q-axis fluxes are given as

$$\lambda_D = \lambda_p \text{ and } \lambda_Q = 0 \tag{74}$$

where λ_p is the peak value of the fundamental frequency flux component. Considering the three-phase symmetry, the flux linkage due to the common component of flux of phase a is only analyzes and it is given as

$$\lambda_a = \lambda_d \cos\psi - \lambda_q \sin\psi \tag{75}$$

In order to obtain the common component of the flux linkage with kth coil at $\psi = 90°$, it is sufficient to only evaluate the q-axis flux components. Evaluating the q-axis flux components of individual VSCs and taking their average [11], [22] gives

$$N\phi_{a_k,l} \mid_{\psi=90°} = \Delta\lambda_{q,avg} \mid_{\psi=90°} = \frac{V_{dc}}{18f_c}\Big(\frac{2}{3} - \frac{\sqrt{3}M}{4}\Big) \tag{76}$$

similarly, the ripple component of the common flux component at $\psi = 0°$ is obtained by evaluating only the d-axis flux component of individual VSCs and taking the average. For $M > 4/9$, it is given as

$$\Delta\lambda_{d,avg} \mid_{\psi=0°} = \frac{V_{dc}}{3f_c}\Big(\frac{5M}{8} - \frac{9M^2}{32} - \frac{1}{3}\Big) \tag{77}$$

Using (77), the worst case value of the common flux component $\phi_{a_k,l_{max}}$ is evaluated.

ACKNOWLEDGMENT

REFERENCES

[1] M. Baumann and J. Kolar, "Parallel connection of two three-phase three-switch buck-type unity-power-factor rectifier systems with dc-link current balancing," *IEEE Trans. Ind. Electron.*, vol. 54, no. 6, pp. 3042–3053, 2007.

[2] B. Andresen and J. Birk, "A high power density converter system for the gamesa G10x 4,5 MW wind turbine," in *Proc. European Conference on Power Electronics and Applications, 2007*, Sept 2007, pp. 1–8.

[3] H. Zhang and L. Tolbert, "Efficiency impact of silicon carbide power electronics for modern wind turbine full scale frequency converter," *IEEE Trans. Ind. Electron.*, vol. 58, no. 1, pp. 21–28, Jan 2011.

[4] "Technical guidline: Generating plants connected to the medium-voltage network." BDEW Bundesverband der Energie- und Wasserwirtschaft e.V., [Online]. Available: http://www.bdew.de, 2008.

[5] J. Muhlethaler, M. Schweizer, R. Blattmann, J. Kolar, and A. Ecklebe, "Optimal design of LCL harmonic filters for three-phase pfc rectifiers," *IEEE Trans. Power Electron.*, vol. 28, no. 7, pp. 3114–3125, 2013.

[6] M. Liserre, R. Cardenas, M. Molinas, and J. Rodriguez, "Overview of multi-MW wind turbines and wind parks," *IEEE Trans. Ind. Electron.*, vol. 58, no. 4, pp. 1081–1095, April 2011.

[7] S. Miller, T. Beechner, and J. Sun, "A comprehensive study of harmonic cancellation effects in interleaved three-phase VSCs," in *Proc. IEEE Power Electronics Specialists Conference, 2007. PESC 2007.*, 2007, pp. 29–35.

[8] L. Asiminoaei, E. Aeloiza, P. N. Enjeti, and F. Blaabjerg, "Shunt active-power-filter topology based on parallel interleaved inverters," *IEEE Trans. Ind. Electron.*, vol. 55, no. 3, pp. 1175–1189, 2008.

[9] D. Zhang, F. Wang, R. Burgos, L. Rixin, and D. Boroyevich, "Impact of Interleaving on AC Passive Components of Paralleled Three-Phase Voltage-Source Converters," *IEEE Trans. Power Electron.*, vol. 46, no. 3, pp. 1042–1054, 2010.

[10] J. Prasad and G. Narayanan, "Minimization of grid current distortion in parallel-connected converters through carrier interleaving," *IEEE Trans. Ind. Electron.*, vol. 61, no. 1, pp. 76–91, Jan 2014.

[11] X. Mao, A. Jain, and R. Ayyanar, "Hybrid interleaved space vector PWM for ripple reduction in modular converters," *IEEE Trans. Power Electron.*, vol. 26, no. 7, pp. 1954–1967, 2011.

[12] K. Xing, F. Lee, D. Borojevic, Z. Ye, and S. Mazumder, "Interleaved PWM with discontinuous space-vector modulation," *IEEE Trans. Power Electron.*, vol. 14, no. 5, pp. 906–917, 1999.

[13] Z. Xu, R. Li, H. Zhu, D. Xu, and C. Zhang, "Control of parallel multiple converters for direct-drive permanent-magnet wind power generation systems," *IEEE Trans. Power Electron.*, vol. 27, no. 3, pp. 1259–1270, March 2012.

[14] H. Akagi, A. Nabae, and S. Atoh, "Control strategy of active power filters using multiple voltage-source PWM converters," *IEEE Trans. Ind. Appl.*, vol. IA-22, no. 3, pp. 460–465, 1986.

[15] F. Ueda, K. Matsui, M. Asao, and K. Tsuboi, "Parallel-connections of pulsewidth modulated inverters using current sharing reactors," *IEEE Trans. Power Electron.*, vol. 10, no. 6, pp. 673–679, Nov 1995.

[16] I. G. Park and S. I. Kim, "Modeling and analysis of multi-interphase transformers for connecting power converters in parallel," in *Proc. of 28th Annual IEEE Power Electronics Specialists Conference, 1997. PESC '97*, vol. 2, Jun 1997, pp. 1164–1170 vol.2.

[17] F. Forest, T. Meynard, E. Laboure, V. Costan, E. Sarraute, A. Cuniere, and T. Martire, "Optimization of the supply voltage system in interleaved converters using intercell transformers," *IEEE Trans. Power Electron.*, vol. 22, no. 3, pp. 934–942, 2007.

[18] F. Forest, E. Laboure, T. Meynard, and V. Smet, "Design and comparison of inductors and intercell transformers for filtering of PWM inverter output," *IEEE Trans. Power Electron.*, vol. 24, no. 3, pp. 812–821, 2009.

[19] J. Salmon, J. Ewanchuk, and A. Knight, "PWM inverters using split-wound coupled inductors," *IEEE Trans. Ind. Appl.*, vol. 45, no. 6, pp. 2001–2009, 2009.

[20] R. Hausmann and I. Barbi, "Three-phase dc-ac converter using four-state switching cell," *IEEE Trans. Power Electron.*, vol. 26, no. 7, pp. 1857–1867, July 2011.

[21] D. Zhang, F. Wang, R. Burgos, and D. Boroyevich, "Total flux minimization control for integrated inter-phase inductors in paralleled, interleaved three-phase two-level voltage-source converters with discontinuous space-vector modulation," *IEEE Trans. Power Electron.*, vol. 27, no. 4, pp. 1679–1688, 2012.

[22] G. Gohil, R. Maheshwari, L. Bede, T. Kerekes, R. Teodorescu, M. Liserre, and F. Blaabjerg, "Modified discontinuous PWM for size reduction of the circulating current filter in parallel interleaved converters," *IEEE Trans. Power Electron.*, vol. 30, no. 7, pp. 3457–3470, July 2015.

[23] G. Gohil, L. Bede, R. Teodorescu, T. Kerekes, and F. Blaabjerg, "Design of the trap filter for the high power converters with parallel interleaved VSCs," in *Proc. 40th Annual Conference on IEEE Industrial Electronics Society, IECON 2014*, Oct 2014, pp. 2030–2036.

[24] G. Gohil, L.Bede, R.Teodorescu, T. Kerekes, and F. Blaabjerg, "Line filter design of parallel interleaved VSCs for high power wind energy conversion system," *IEEE Trans. Power Electron.*, [Online early access], DOI: 10.1109/TPEL.2015.2394460, 2015.

[25] G. Gohil, L. Bede, R. Maheshwari, R. Teodorescu, T. Kerekes, and F. Blaabjerg, "Parallel interleaved VSCs: influence of the PWM scheme on the design of the coupled inductor," in *Proc. 40th Annual Conference on IEEE Industrial Electronics Society, IECON 2014*, Oct 2014, pp. 1693–1699.

Ghanshyamsinh Gohil (S'13) received the M.Tech. degree in electrical engineering with specialization in power electronics and power systems from the Indian Institute of Technology-Bombay, Mumbai, India, in 2011.

He is currently working towards the Ph.D. degree at the Department of Energy Technology, Aalborg University, Denmark. Prior to joining the Ph.D. studies, he was employed at Siemens Corporate Technology, Bangalore. His research interests include parallel operation of voltage source converters, pulsewidth modulation techniques and the design of the inductive power components.

Lorand Bede (S'11) was born in Romania in 1989. He received the engineering degree in electrical engineering from Sapientia Hungarian University of Transilvania, Trgu Mure, Romania, 2011,the MSc. degree in Power Electronics and Drives from Aalborg University, Aalborg, Denmark, in2013. Currently he is a PhD Fellow at the Departmen t of Energy Technology, at Aalborg University,Aalborg. His research interest include grid connected applications based on parallel interleaved converters for wind turbine applications.

Remus Teodorescu (S'94-A'97-M'99-SM'02-F'12) received the Dipl.Ing. degree in electrical engineering from Polytechnical University of Bucharest, Romania in 1989, and PhD. degree in power electronics from University of Galati, Romania, in 1994. In 1998, he joined Aalborg University, Department of Energy Technology, power electronics section where he currently works as full professor. Since 2013 he is a visiting professor at Chalmers University. He has coauthored the book Grid Converters for Photovoltaic and Wind Power Systems, ISBN: 978-0-470-05751-3, Wiley 2011 and over 200 IEEE journals and conference papers. His areas of interests includes: design and control of grid-connected converters for photovoltaic and wind power systems, HVDC/FACTS based on MMC, SiC-based converters, storage systems for utility based on Li-Ion battery technology. He was the coordinator of the Vestas Power Program 2008 2013.

Tamas Kerekes (S'06-M'09) obtained his Electrical Engineer diploma in 2002 from Technical University of Cluj, Romania, with specialization in Electric Drives and Robots. In 2005, he graduated the Master of Science program at Aalborg University, Institute of Energy Technology in the field of Power Electronics and Drives. In Sep. 2009 he obtained the PhD degree from the Institute of Energy Technology, Aalborg University. The topic of the PhD program was: "Analysis and modeling of transformerless PV inverter systems". He is currently employed as an Associate professor and is doing research at the same institute within the field of grid connected renewable applications. His research interest include grid connected applications based on DC-DC, DC-AC single- and three-phase converter topologies focusing also on switching and conduction loss modeling and minimization in case of Si and new wide-bandgap devices.

Frede Blaabjerg (S'86-M'88-SM'97-F'03) was with ABB-Scandia, Randers, Denmark, from 1987 to 1988. From 1988 to 1992, he was a Ph.D. Student with Aalborg University, Aalborg, Denmark. He became an Assistant Professor in 1992, an Associate Professor in 1996, and a Full Professor of power electronics and drives in 1998. His current research interests include power electronics and its applications such as in wind turbines, PV systems, reliability, harmonics and adjustable speed drives. He has received 15 IEEE Prize Paper Awards, the IEEE PELS Distinguished Service Award in 2009, the EPE-PEMC Council Award in 2010, the IEEE William E. Newell Power Electronics Award 2014 and the Villum Kann Rasmussen Research Award 2014. He was an Editor-in-Chief of the IEEE TRANSACTIONS ON POWER ELECTRONICS from 2006 to 2012. He has been Distinguished Lecturer for the IEEE Power Electronics Society from 2005 to 2007 and for the IEEE Industry Applications Society from 2010 to 2011. He is nominated in 2014 by Thomson Reuters to be between the most 250 cited researchers in Engineering in the world.